Manufacturing Letters 13 (2017) 15–20

Contents lists available at ScienceDirect

Manufacturing Letters

journal homepage: www.elsevier.com/locate/mfglet

Letters

Quality part production via multi-laser additive manufacturing

Mohammad Masoomi, Scott M. Thompson *, Nima Shamsaei

Laboratory for Fatigue & Additive Manufacturing Excellence (FAME), Department of Mechanical Engineering, Auburn University, Auburn, AL 36849, United States

ARTICLE INFO

Article history:
Received 24 December 2016
Received in revised form 9 May 2017
Accepted 25 May 2017
Available online 27 May 2017

Keywords:
Powder bed fusion
Ti-6Al-4V
Heat transfer
Residual stress
Scan strategy

ABSTRACT

Multi-Laser Powder Bed Fusion (ML-PBF), a metals additive manufacturing (AM) method, provides an opportunity to produce more parts in less time. However, the effects of using multiple, moving energy sources on sintered part integrity, as well as the transferability between process parameters developed for L-PBF and ML-PBF, remains unknown. Via validated simulations, this study provides insight into how various single- and multi-laser PBF scan strategies can impact powder/part heat affected zones (HAZs), melt pool temperatures and local temperature gradient magnitudes, which affect microstructural properties, defect statistics, and mechanical behavior of fabricated parts.

1. Introduction

Laser Powder Bed Fusion (L-PBF) is an additive manufacturing (AM) method used for fabricating metallic components via directed laser energy and a pre-deposited layer (or 'bed') of powder [1]. Many industries, ranging from aerospace to biomedical, are employing L-PBF for small lot production of precious components due to it providing the ability to reduce part assembly joints, manufacture remotely, obtain customized/complex-geometry parts and more [2,3]. However, before L-PBF parts can be reliably used in application, their quality must be assured for each newly-developed AM system, powder source and operating/design parameter group [4,5]. It is currently common practice for one to seek 'process-structure-property-performance' relationships inherent to a specific material/feedstock and process to enable the fabrication of parts with target geometry, density and mechanical performance.

Residual stress within L-PBF metal parts can be significant due to the locality and speed of the fusion process in which they were made. Since a part's geometric tolerance and mechanical integrity are coupled with its residual stress distribution (e.g. warping), the spatiotemporal temperature fields/gradients realized during manufacture conducive for such distributions are worthy of investigation. Residual stress formation is indirectly related to local, spatial variation in cooling rates and/or temperature, i.e. temperature gradients, experienced during directed energy AM [6,7] and can be mitigated via support/anchor design and/or using appropriate laser scan strategies (i.e. scan direction with respect to time) [8,9]. Parry et al. demonstrated via thermo-mechanical simulation that residual stresses in PBF parts are anisotropic due to non-uniform thermal history and typically increase with longer tracks [9]. Cheng et al. [10] and Nickel et al. [11] numerically demonstrated that dividing individual layers into 'islands' with dedicated, rotating scan patterns can result in PBF parts possessing a more homogeneous residual stress distribution.

Multi-laser PBF (ML-PBF) is an emerging technology [12–14] driven by the demand to reduce part production times associated with conventional L-PBF processes, which can take several hours to complete a single build [15]. Although research into the use of multiple lasers during welding and cladding has been investigated [15–19], the effects of multiple energy sources during PBF on subsequent part integrity have not been widely disseminated. The ability to transfer known/developed process parameters and scan patterns for effective, single-laser PBF to ML-PBF is at question. The aim of this research letter is to provide the AM community insights into effective laser scan planning for ML-PBF, and to relate such insights to conventional, single-laser PBF strategies.

2. Numerical methodology and validation

Simulation of the L-PBF process significantly reduces the time and feedstock invested for determining effective process/design parameter groups for a given material. To maintain efficient computational investment, the L-PBF process must be idealized and the

---

* Corresponding author at: 1418 Wiggins Hall, 354 War Eagle Way, Auburn, AL 36849, United States.

E-mail address: smthompson@auburn.edu (S.M. Thompson).

http://dx.doi.org/10.1016/j.mfglet.2017.05.003

governing equations for heat diffusion discretized and solved by finite difference [20–25]. The powder bed and solidified part may be represented as continua with effective density and transport properties, and this approach is adopted herein. Due to the brevity of this letter, the reader is referred to Ref. [25] for a more rigorous description of the modeling schemes and numerical methods employed.

The spatiotemporal temperature field encompassing the substrate, powder bed, solidified part and melt pool was estimated by discretizing and numerically solving the heat equation via finite difference. Simulations were performed using the commercially-available software COMSOL Multiphysics® 5.1 in conjunction with custom coding scripts. Temperature-dependent properties of solid- and liquid-phase Ti-6Al-4V [26] and a liquid/solid Ti–6Al–4V absorptance of 0.25 [27] were employed. The L-PBF argon shielding gas flow rate was assumed to be 167 cm^3/s [23] with temperature-dependent properties taken from Lemmon et al. [28]. The powder bed porosity was assumed to be 0.4 – typical of many L-PBF systems [9]. Ti-6Al-4V was selected as the process material due to its often-desired mechanical properties [29] and applicability to the biomedical, astronautical and aerospace industries [29]. All simulations involved a Ti-6Al-4V substrate with an initial temperature of 20 °C. Time was discretized into equal time steps of $\Delta t = 600\ \mu s$ and the employed mesh possessed cell widths no less than 20 μm. Utilized mesh and time discretization schemes were found to provide relatively mesh/time-step independent solutions for temperature [25].

The numerical model was validated by simulating the L-PBF process described by Yadroitsev et al. [30] which focused on recording the temperature response (via a CCD camera) of gas-atomized Ti–6Al–4V powder solidifying during a single laser pass. The maximum Ti-6Al-4V melt pool temperatures during the melting of a single track as predicted from the simulation, and as reported from experimentation by Yadroitsev et al. [30], were found and compared. For various laser powers investigated, the percent relative error was found to always be less than or equal to 3%.

The validated numerical model was used for simulating the L-PBF or ML-PBF of a two-layer, $10 \times 5 \times 0.08\ mm^3$ Ti–6Al–4V parallelepiped to demonstrate the effects of layer number, island division scheme, laser sweep direction and laser number (i.e. ML-PBF vs. L-PBF) on simulated heat affected zones (HAZs), melt pool temperatures and local temperature gradient magnitudes. To present mechanically-relevant results, the L-PBF process parameters/conditions as reported by Vilaro et al. [31], were utilized as they proved effective in producing 99% dense Ti–6Al–4V specimens (via a Trumpf LF250 L-PBF system).

In total, eleven different simulations, i.e. S1-S11, were performed and are summarized in Table 1. Fig. 1 illustrates the various scan patterns (SPs) and island division schemes (i.e. 'quadrant' and 'fourths') investigated for one and four lasers; referred to now as SP-A, SP-B, and so forth, until SP-H, corresponding to Fig. 1(a)–(h), respectively. Scan strategies were held constant for each layer (no rotation) and were selected as to possess unidirectional tracks collinear with the X-Y axes, 'sweeping' in either the X+ or Y+ directions. The order/sequence in which islands were built using a single laser consisted of fabricating the top-left quadrant, i.e. Q1, followed by Q2, and so forth, in a clockwise fashion. In order to characterize the spatiotemporal temperature distribution along each layer of the Ti-6Al-4V parallelepiped during its L-PBF, sixteen (static) points, i.e. P1-P16, were imposed along each layer for extraction of results. Each 'extraction point' was centered within a sixteenth of the parallelepiped as shown schematically in Fig. 1 (i). The distance between each point was 2.5 mm in the X-direction and 1.25 mm in the Y-direction. Lasers were assumed identical in intensity profile and power while operating synchronously for all ML-PBF simulations conducted.

3. Results and discussion

Representative melt pool and HAZ temperature contours, at a location along the middle of a track within the first layer, for S1, S3 and S4, are shown in Fig. 2(a)–(c), respectively; while a magnified view of a melt pool is provided in Fig. 2(a). As one would expect, the ML-PBF process results in a larger cross-section of material having elevated temperature due to multiple directed energy sources. Melt pool temperature distributions were found to be similar during the majority of ML-PBF layer fabrication due primarily to the locality of laser irradiation and since the powder bed (and substrate) contains a much higher thermal capacitance (due to its volume). For smaller powder bed and/or part volumes, or more convergent scan patterns, e.g. S11, HAZ temperature distributions become more biased to surrounding lasers due to their proximity over longer periods of time.

When using multiple lasers, the powder bed receives more energy in a shorter amount of time and track lengths are reduced; thus, there is less time for thermal energy to diffuse in between tracks, and local temperatures can be higher. For example, as shown in Fig. 2(b), the quadrant island division scheme has a more discernable level of pre-heat ahead of the melt pools. The melt pool temperatures were found to peak around ∼2850 °C; however, these maximum temperatures should be slightly less due to melt pool convection effects.

In general, parts made via L-PBF experience very high temperature gradients, and this can be a pre-cursor to residual stress formation if such gradients correspond to a solid point that will not re-melt [32,33]. An average of the maximum temperature gradient magnitude, extracted at each point P1-P16 along the M^{th} layer, i.e. $AMTG_M$, was calculated for S1-S11 using:

$$AMTG_M = \frac{1}{16}\sum_{i=1}^{16}(\max\|\nabla T_i\|) \quad (1)$$

Table 1
List and description of simulations conducted for the single- and multi-laser PBF of the 2-layered Ti-6Al-4V parallelepiped.

Simulation #	Scan pattern	# lasers	# islands	Island splitting scheme	Island sequence	# sub-islands	Sub-island sequence	Track sweep direction
S1	SP-A	1	1	Full	All at once	0	N/A	Y+
S2	SP-C	1	4	Quadrant	Q1, Q2, Q3, Q4	0	N/A	Y+
S3	SP-C	4	4	Quadrant	All at once	0	N/A	Y+
S4	SP-F	4	4	Fourths (X)	All at once	0	N/A	Y+
S5	SP-B	1	1	Full	All at once	0	N/A	X+
S6	SP-D	1	4	Quadrant	Q1, Q2, Q3, Q4	0	N/A	X+
S7	SP-D	4	4	Quadrant	All at once	0	N/A	X+
S8	SP-G	4	4	Fourths (Y)	All at once	0	N/A	X+
S9	SP-E	1	4	Quadrant	Q1, Q2, Q3, Q4	0	N/A	Y+, X+, Y−, X−
S10	SP-E	4	4	Quadrant	All at once	0	N/A	Y+, X+, Y−, X−
S11	SP-H	4	4	Quadrant	All at once	16	Q1, Q2, Q3, Q4	Y+, X+, Y−, X−

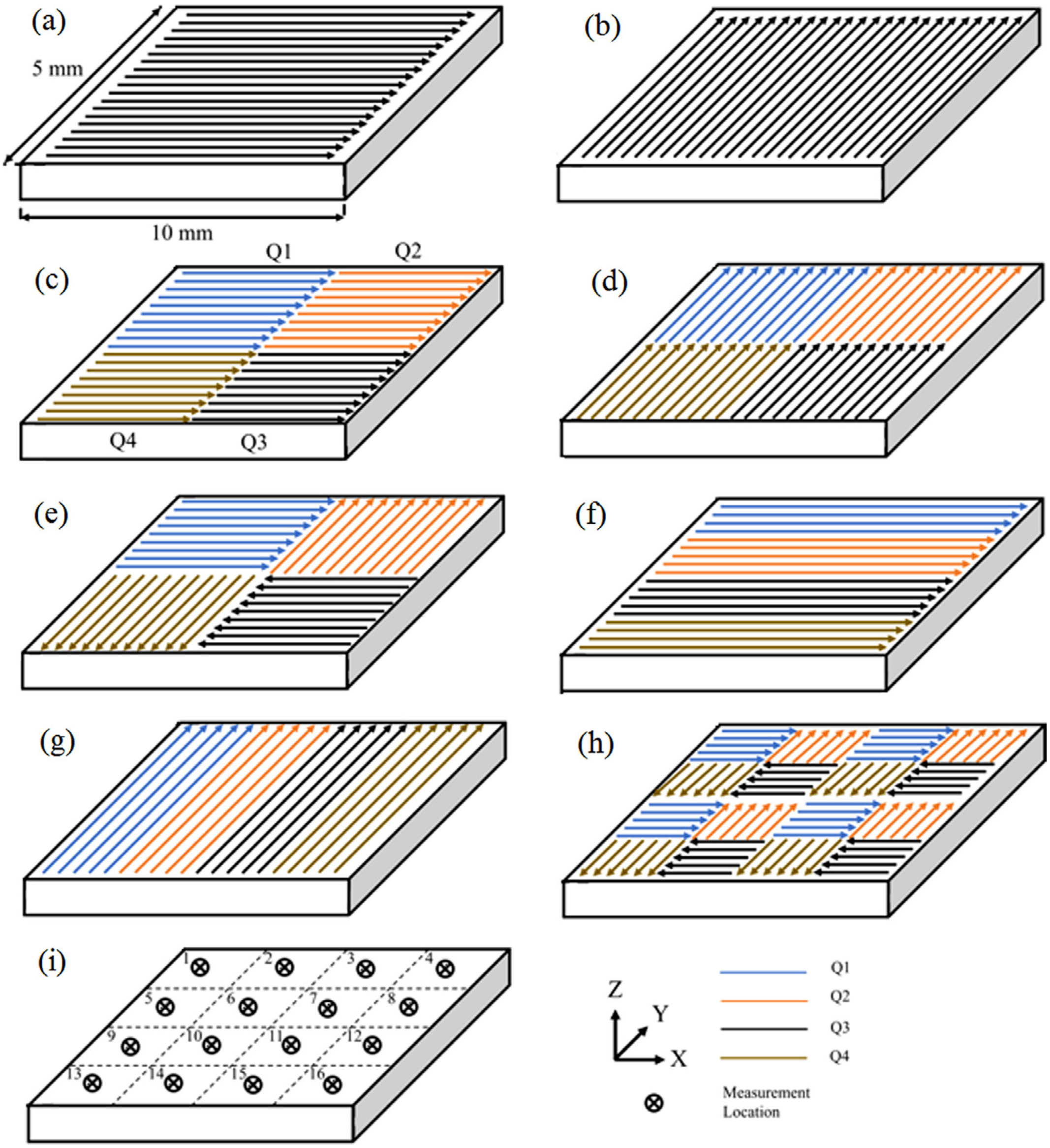

Fig. 1. (a)-(h) Schematic of scan strategies and island division schemes employed for simulations S1-S11, (i) temperature measurement locations along a layer (unity aspect ratio for illustration purposes only).

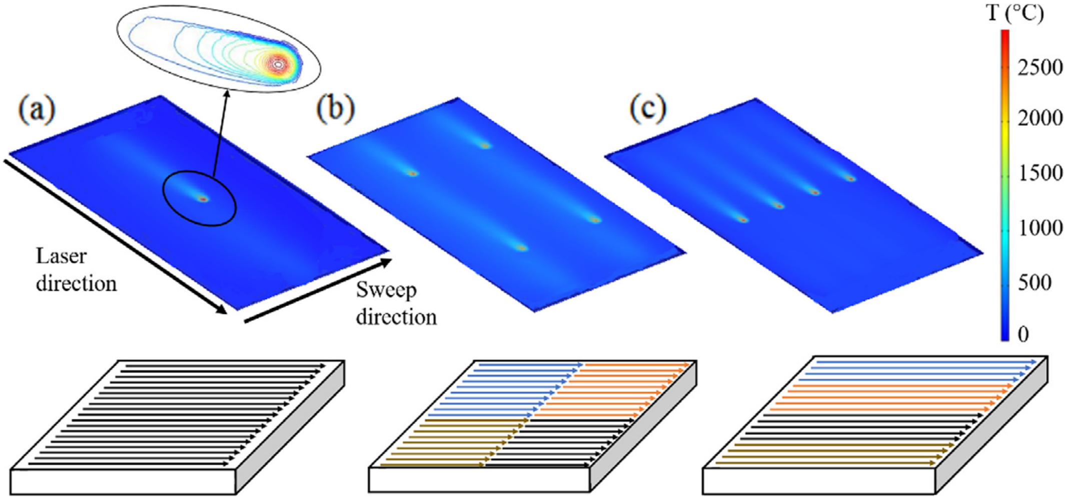

Fig. 2. Scan strategies and respective temperature response of Ti-6Al-4V powder bed and part during fabrication of (a) S1, (b) S3 and (c) S4.

In addition, the homogeneity of AMTGs along a layer was quantified by taking their standard deviation, i.e. the SDTG_M:

$$\mathrm{SDTG}_M = \sqrt{\sum_{i=1}^{16} \left(\max \|\nabla T_i\| - \mathrm{AMTG}_M\right)^2 / 15} \qquad (2)$$

The AMTGs for the first and second layers during S1-S11 are shown in Fig. 3(a). It may be seen that AMTGs and SDTGs are generally lower (>50%) during fabrication of the second layer which has less thermal interaction with the substrate material. This first layer is typically sacrificial upon completion of PBF, while the second layer temperature response is more representative of those inherent to subsequent layers. The AMTG varies with location; being higher at points closer to the start of a track and decreasing along the track length due to heat accumulation effects. The temperature gradient magnitude also decreases with laser track sweep direction, meaning, as the part solid volume increases and the surrounding media accumulates excess heat, later tracks will experience lower AMTGs.

By comparing the AMTGs between S2 and S3, as well as S6 and S7, in Fig. 3(a), it may be seen that employing four lasers via ML-PBF reduces average temperature gradient magnitudes by ~5%. A ~10% reduction in AMTG is achieved by employing the 'fourths' island division scheme instead of the 'quadrant' scheme. Results

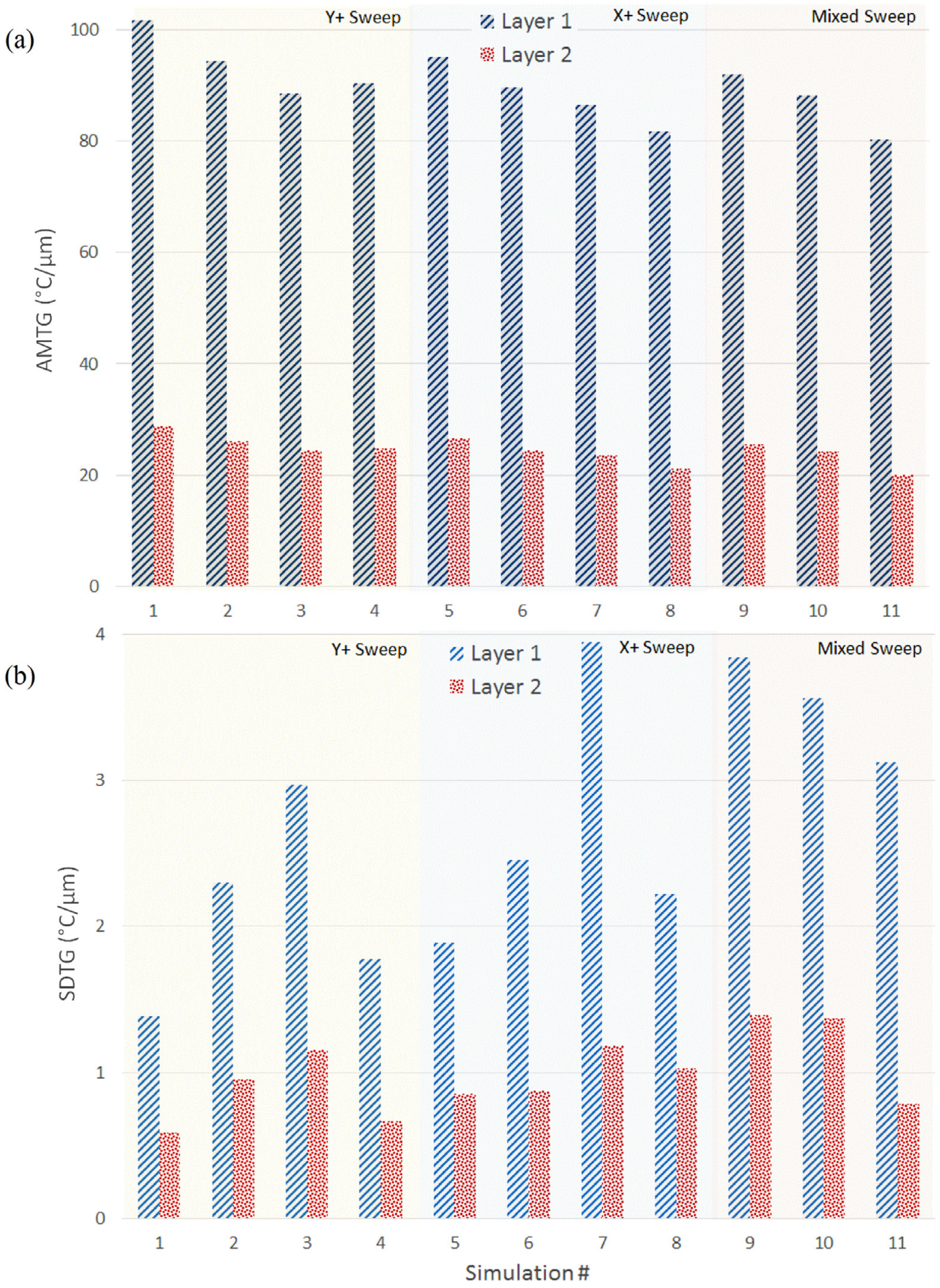

Fig. 3. (a) Average, maximum temperature gradient (AMTG) and its (b) standard deviation (SDTG) with respect to first and second layers of the Ti-6Al-4V parallelepiped during its single- or multi-laser PBF following scan strategies described in S1-S11.

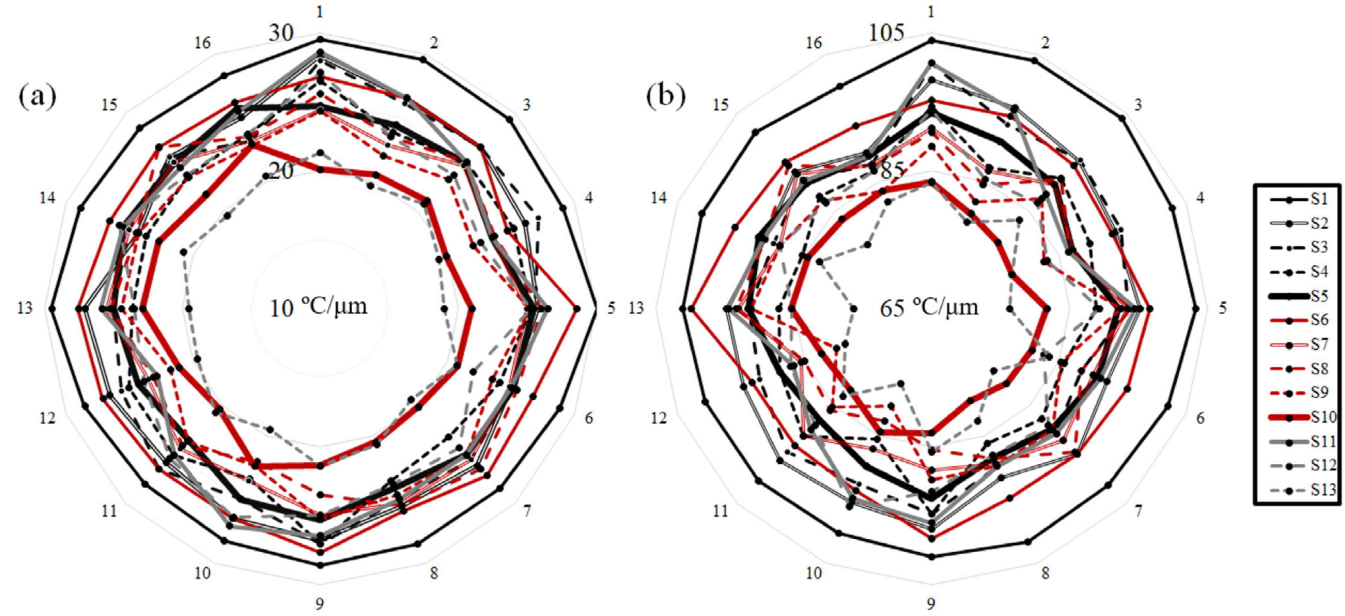

Fig. 4. Radar chart showing the maximum temperature gradients measured at points P1-P16 (circumferential markings) during manufacture of the Ti-6Al-4V parallelepiped following scan strategies described in S1-S11 (star/circular profiles) for the (a) second layer and (b) first layer.

indicate that building a layer while employing a sequenced island strategy decreases the AMTG (i.e. S1 vs. S2, S5 vs. S6, S10 vs. S11) for both layers. Lower AMTGs existed when lasers were swept in the X-direction, along the longest dimension of the parallelepiped, with tracks parallel to the shortest edge. Mixed-sweeping techniques appear to provide the lowest AMTG when using four lasers.

The spatial uniformity of the AMTG for a given layer, as quantified via the SDTG, provides insight into the residual stress distribution, with higher SDTGs suggesting a temperature response more conducive to residual stress formation. Fig. 3(b) provides the SDTGs for the various scan strategies investigated, while Fig. 4 provides radar charts of the AMTGs. The radar charts provide an alternate means to visualize the uniformity in temperature gradients along each layer and can assist one during scan planning. For instance, S1 was found to provide the lowest SDTG, and this results in a more circular shape within the radar chart, while S7 and S9, for example, have more star-shaped profiles due to their higher SDTGs. In general, strategies conducive for lower AMTGs are found to possess less spatial homogeneity in AMTGs, as evidenced by them having higher SDTGs. For example, S1, S5 and S9 provide for the highest AMTG for their respective sweep strategy (for both layers), while in contrast, these same strategies possess the lowest SDTG in their category. Lower SDTGs, unlike the AMTG, were found to exist when sweeping lasers in the Y+direction, along the shortest dimension of the parallelepiped, with tracks parallel to the longest edge. Mixed-sweeping techniques demonstrated to provide the highest SDTG when using one or four lasers.

Results suggest that increasing the number of islands/sub-islands (e.g. S1 to S2 to S11), for a unidirectional sweeping strategy and a single laser, will decrease the AMTG and increase the SDTG of a layer. Increasing the laser number, while holding the number of islands constant, while employing the quadrant division scheme, will further increase the SDTG for unidirectional sweeping strategies. However, utilizing an island division scheme cognizant of the part shortest edge can provide a significant reduction in SDTG. For instance, the 'fourths' island division scheme that provides for adjacent, equally-sized islands along a single direction of the part, appears to be more appropriate for the multi-laser approach. For such island division schemes, the SDTG is more comparable to that experienced for a unit-island layer, yet the production time is greatly increased. As seen in Fig. 2, the temperature footprint surrounding the melt pools is hotter for the quadrant division scheme than it is for the fourths division scheme. The mixed sweep approach for accomplishing single- (i.e. S9) or multi-laser PBF (i.e. S10 and S11) provides less homogeneity in AMTGs; however, the lowest AMTG was accomplished using this approach combined with sub-islands for ML-PBF (i.e. S11). The mixed-sweep strategy (i.e. SP-E, SP-H), in contrast to both the X and Y scan strategies (i.e. SP-A through SP-D), decreases in SDTG as more islands and lasers are introduced.

4. Conclusions

The temperature response during the multi-laser powder bed fusion (ML-PBF) of Ti-6Al-4V was simulated to provide guidance in scan planning toward minimizing residual stress and enhancing mechanical performance of fabricated parts. Effects of laser number and sweep direction were investigated for a rectangular, 2-layered part. In using multiple lasers, the time required for fabricating each layer decreases significantly – by ~75% when using 4 lasers. Preliminary results indicate that the melt pool peak temperature is insensitive, while temperature gradient magnitudes are extremely sensitive, to scan strategy and number of lasers. The average magnitude of peak temperature gradients experienced, and thus the general level of residual stress expected, along a layer can be reduced by employing island-division schemes, and even more, using multiple lasers. However, such strategies can result in the part having non-uniform, anisotropic residual stress distributions, ultimately affecting its mechanical/fatigue strength. Unidirectional scan strategies with tracks perpendicular, and unit-row islands distributed parallel, to a part's longest edge can also reduce maximum temperature gradients. Obtaining a uniform residual stress distribution appears to be highly dependent on island geometry/distribution, as well as the orientation of laser scan vectors between adjacent islands. Since the optimal scan strategy, consisting of scan path directions and island division scheme/sequencing, will depend on layer dimensions and the number, wavelength, synchronicity, power, and speed of other lasers, additional work must be conducted, both computationally and experimentally, to elucidate more process-structure-property-performance relationships for various machine environments, materials and constraints.

Acknowledgement

This work has been supported by the National Science Foundation under Grant No. 1657195.

References

[1] Deckard CR. Method and apparatus for producing parts by selective sintering. US 4863538 A; 1989.

[2] Wang X, Xu S, Zhou S, Xu W, Leary M, Choong P, et al. Topological design and additive manufacturing of porous metals for bone scaffolds and orthopaedic implants: a review. Biomaterials 2016;83:127–41. http://dx.doi.org/10.1016/j.biomaterials.2016.01.012.

[3] Frazier WE. Metal additive manufacturing: a review. J Mater Eng Perform 2014;23:1917–28. http://dx.doi.org/10.1007/s11665-014-0958-z.

[4] Yadollahi A, Shamsaei N. Additive manufacturing of fatigue resistant materials: challenges and opportunities. Int J Fatigue 2017;98:14–31. http://dx.doi.org/10.1016/j.ijfatigue.2017.01.001.

[5] Shamsaei N, Yadollahi A, Bian L, Thompson SM. An overview of Direct Laser Deposition for additive manufacturing; Part II: Mechanical behavior, process parameter optimization and control. Addit Manuf 2015;8:12–35. http://dx.doi.org/10.1016/j.addma.2015.07.002.

[6] Vora P, Mumtaz K, Todd I, Hopkinson N. AlSi12 in-situ alloy formation and residual stress reduction using anchorless selective laser melting. Addit Manuf 2015;7:12–9. http://dx.doi.org/10.1016/j.addma.2015.06.003.

[7] Prabhakar P, Sames WJ, Dehoff R, Babu SS. Computational modeling of residual stress formation during the electron beam melting process for Inconel 718. Addit Manuf 2015;7:83–91. http://dx.doi.org/10.1016/j.addma.2015.03.003.

[8] Heigel JC, Michaleris P, Reutzel EW. Thermo-mechanical model development and validation of directed energy deposition additive manufacturing of Ti-6Al-4V. Addit Manuf 2015;5:9–19. http://dx.doi.org/10.1016/j.addma.2014.10.003.

[9] Parry L, Ashcroft IA, Wildman RD. Understanding the effect of laser scan strategy on residual stress in selective laser melting through thermo-mechanical simulation. Addit Manuf 2016;12:1–15. http://dx.doi.org/10.1016/j.addma.2016.05.014.

[10] Cheng B, Shrestha S, Chou K. Stress and deformation evaluations of scanning strategy effect in selective laser melting. Addit Manuf 2016. http://dx.doi.org/10.1016/j.addma.2016.05.007.

[11] Nickel AH, Barnett DM, Prinz FB. Thermal stresses and deposition patterns in layered manufacturing. Mater Sci Eng, A 2001;317:59–64. http://dx.doi.org/10.1016/S0921-5093(01)01179-0.

[12] Keremes JJ, Haynes JD, Gao Y, Matejczyk DE. Laser configuration for additive manufacturing, US 20130112672 A1, 2013.

[13] Rockstroh TJ, Gray DC, Cheverton MA, Ostroverkhov VP. Selective laser melting additive manufacturing method with simultaneous multiple melting lasers beams and apparatus therefor, WO 2015191257 A1, 2015.

[14] Fockele M. Device for manufacture of objects by layer-wise constructing from powder-form material has sub-systems of irradiating unit allocated to respective sections of building field on base arrangement, EP1839781 A3, 2006.

[15] Keicher DM, Miller WD. Multiple beams and nozzles to increase deposition rate, US 5993554 A, 2001.

[16] Wiesner A, Schwarze D. Multi-Laser selective laser melting. In: 8th Int. Conf. Photonic Technol., Fürth, Germany, 2014.

[17] Williams NF. Endoprosthesis having multiple laser welded junctions method and procedure, US 5716396 A, 1998.

[18] Hu Y, Hehmann WF. Multi-laser beam welding high strength superalloys, US 6972390 B2, 2005.

[19] Benda JA, Parasco A. Apparatus for multiple beam laser sintering, US5508489 A, 1996.

[20] Li Y, Gu D. Thermal behavior during selective laser melting of commercially pure titanium powder: numerical simulation and experimental study. Addit Manuf 2014;1:99–109. http://dx.doi.org/10.1016/j.addma.2014.09.001.

[21] Masmoudi A, Bolot R, Coddet C. Investigation of the laser–powder–atmosphere interaction zone during the selective laser melting process. J Mater Process Technol 2015;225:122–32. http://dx.doi.org/10.1016/j.jmatprotec.2015.05.008.

[22] Verhaeghe F, Craeghs T, Heulens J, Pandelaers L. A pragmatic model for selective laser melting with evaporation. Acta Mater 2009;57:6006–12. http://dx.doi.org/10.1016/j.actamat.2009.08.027.

[23] Masoomi M, Shamsaei N, Gao X, Thompson SM, Elwany A, Bian L. Modeling, simulation and experimental validation of heat transfer during selective laser melting. In: ASME 2015 Int. Mech. Eng. Congr. Expo., ASME, Houston, Texas, USA, 2015: p. V02AT02A007. doi: 10.1115/IMECE2015-52165.

[24] Masoomi M, Thompson SM, Shamsaei N, Elwany A, Bian L. An experimental-numerical investigation of heat transfer during selective laser melting. In: 26th Int. Solid Free. Fabr. Symp. – An Addit. Manuf. Conf., Austin, 2015: p. 229.

[25] Masoomi M, Thompson SM, Shamsaei N. Laser powder bed fusion of Ti-6Al-4V parts: thermal modeling and mechanical implications. Int J Mach Tools Manuf 2017;118–119:73–90. http://dx.doi.org/10.1016/j.ijmachtools.2017.04.007.

[26] Neira Arce A. Thermal modeling and simulation of electron beam melting for rapid prototyping on Ti6Al4V alloys, North Carolina State University, 2012.

[27] Fischer P, Romano V, Weber HP, Karapatis NP, Boillat E, Glardon R. Sintering of commercially pure titanium powder with a Nd:YAG laser source. Acta Mater 2003;51:1651–62. http://dx.doi.org/10.1016/S1359-6454(02)00567-0.

[28] Lemmon EW, Jacobsen RT. Viscosity and thermal conductivity equations for nitrogen, oxygen, argon, and air. Int J Thermophys 2004;25:21–69. http://dx.doi.org/10.1023/B:IJOT.0000022327.04529.f3.

[29] Kumar P, Bajpai V, Singh R. Burr height prediction of Ti6Al4V in high speed micro-milling by mathematical modeling. Manuf Lett 2017;11:12–6.

[30] Yadroitsev I, Krakhmalev P, Yadroitsava I. Selective laser melting of Ti6Al4V alloy for biomedical applications: Temperature monitoring and microstructural evolution. J Alloys Compd 2014;583:404–9. http://dx.doi.org/10.1016/j.jallcom.2013.08.183.

[31] Vilaro T, Colin C, Bartout JD. As-fabricated and heat-treated microstructures of the Ti-6Al-4V alloy processed by selective laser melting. Metall Mater Trans A 2011;42:3190–9. http://dx.doi.org/10.1007/s11661-011-0731-y.

[32] Mercelis P, Kruth J-PJ. Residual stresses in selective laser sintering and selective laser melting. Rapid Prototyp J 2006;12:254–65. http://dx.doi.org/10.1108/13552540610707013.

[33] Paul R, Anand S, Gerner F. Effect of thermal deformation on part errors in metal powder based additive manufacturing processes. J Manuf Sci Eng 2014;136:31009. http://dx.doi.org/10.1115/1.4026524.